Periodic variability of the mainline hydroxyl masers in G9.62+0.20E

S. Goedhart [1,2]★ R. van Rooyen,[1,2] D. J. van der Walt,[2] J. P. Maswanganye,[2]
A. Sanna,[3] G. C. MacLeod[4,5] and S. P. van den Heever[4]

[1]*South African Radio Astronomy Observatory, 2 Fir Street, Black River Park, Observatory 7925, South Africa*
[2]*Center for Space Research, North-West University, Potchefstroom Campus, Private Bag X6001, Potchefstroom 2520, South Africa*
[3]*Max-Planck-Institut für Radioastonomie, Auf dem Hügel 69, D-53121 Bonn, Germany*
[4]*Hartebeesthoek Radio Astronomy Observatory, PO Box 443, Krugersdorp 1740, South Africa*
[5]*The University of Western Ontario, 1151 Richmond Street, London, ON N6A 3K7, Canada*

ABSTRACT
We present the results of a monitoring campaign using the KAT-7 and HartRAO 26 m telescopes, of hydroxyl, methanol, and water vapour masers associated with the high-mass star-forming region G9.62+0.20E. Periodic flaring of the mainline hydroxyl masers was found, similar to that seen in the 6.7 and 12.2 GHz methanol masers. The 1667 MHz flares are characterized by a rapid decrease in flux density, which is coincident with the start of the 12.2 GHz methanol maser flare. The decrease in the OH maser flux density is followed by a slow increase till a maximum is reached after which the maser decays to its pre-flare level. A possible interpretation of the rapid decrease in the maser flux density is presented. Considering the projected separation between the periodic methanol and OH masers, we conclude that the periodic 12.2 methanol masing region is located about 1600 au deeper into the molecular envelope compared to the location of the periodic OH masers. A single water maser flare was also detected, which seems not to be associated with the same event that gives rise to the periodic methanol and OH maser flares.

Key words: masers – ISM: clouds – radio lines: ISM – H II regions – stars: formation.

1 INTRODUCTION

To date, there are at least 20 known periodic methanol masers (Goedhart et al. 2009; Araya et al. 2010; Szymczak et al. 2011; Fujisawa et al. 2014; Goedhart et al. 2014; Maswanganye et al. 2015; Szymczak, Wolak & Bartkiewicz 2015; Maswanganye et al. 2016; Szymczak et al. 2016; Sugiyama et al. 2017) including one source that shows quasi-periodic variations in both methanol and formaldehyde (Araya et al. 2010). The formaldehyde and methanol variations were simultaneous and showed very close correspondence to each other, which the authors speculated was due to modulation of the infrared radiation field by periodic accretion in a binary system. Green et al. (2012) found a possible indication of periodic variability in the hydroxyl masers in G12.89+0.49, where the hydroxyl masers may have undergone a periodic drop in intensity. However, their results were not conclusive since the time-series was undersampled. Szymczak et al. (2016) found anticorrelated variations in the water and methanol masers in G107.298+5.639 even though there are good spatial and velocity overlaps between the two masers. Methanol and hydroxyl masers are thought to share a similar (radiative) pump mechanism (Cragg, Sobolev &

Godrey 2002) and are often found in close spatial proximity, while water masers are collisionally pumped and require high-density environments. Thus, correlated variability may be expected between hydroxyl and methanol masers. However, since the two molecules have different energy level structures, they may not necessarily respond in exactly the same way to changes in the pumping radiation field. The fact that several of the periodic methanol maser sources also have associated hydroxyl masers allows us to investigate to what extent the hydroxyl masers also show periodic flaring and therefore to possibly determine whether the flaring is due to changes in the maser amplification or in the background seed photon flux.

A number of known periodic methanol masers were monitored on a weekly basis at 1665 and 1667 MHz as part of the seven-element Karoo Array Telescope (KAT-7) science verification programme. This paper focuses on G9.62+0.20E, which showed clear evidence of variability in the hydroxyl masers during the first year of monitoring. It was subsequently monitored on a daily basis during the expected 2014 June and 2015 February methanol maser flares while simultaneously monitoring the 6.7 and 12.2 GHz methanol and 22.2 GHz water masers using the Hartebeesthoek Radio Astronomy Observatory (HartRAO) 26 m telescope.

G9.62+0.20E is a high-mass star-forming region with a hypercompact H II region harbouring at least one massive star in

★ E-mail: sharmila@ska.ac.za

an early evolutionary phase (Garay et al. 1993). It has a number of masers projected against the H II region – Class II methanol masers, water masers, and hydroxyl masers (Sanna et al. 2015) and is located at a distance of 5.2 kpc from the Sun (Sanna et al. 2009). It was the first methanol maser source discovered to show periodic variations (Goedhart, Gaylard & van der Walt 2003), with a best-fitting period of 243.3 d (Goedhart et al. 2014). Simultaneous flares in methanol have been observed at 6.7, 12.2, and 107 GHz (van der Walt, Goedhart & Gaylard 2009). One explanation of the methanol maser flare profiles is by the variation of the free–free continuum flux in the background H II region due to variable ionizing radiation associated with shocked winds from a colliding wind binary system with a non-zero orbital eccentricity (van der Walt 2011). However, it has been argued by Parfenov & Sobolev (2014) that the same effect can be produced by variations of the dust temperature in an accretion disc around a forming binary system, while Inayoshi et al. (2013) suggest that pulsational instabilities of massive protostars could arise during rapid accretion. Singh & Deshpande (2012) investigated the possibility of bipolar outflows in young binary systems as a possible explanation for some of the periodic methanol masers. See van der Walt et al. (2016) for a further discussion.

The OH monitoring of G9.62+0.20E revealed complex behaviour across multiple OH maser features, with some features showing a pronounced drop in power at the same time that the methanol masers started to flare. Not all of the hydroxyl or methanol maser features flare, and since the relative positions of all the maser species and the background H II region are known (Sanna et al. 2015), the regions undergoing periodic flares can be isolated. It was found that the flaring methanol and OH masers are, in projection, about 1600 au apart. The decay of the flaring OH masers can be described in terms of the variation of the free–free emission from a recombining hydrogen plasma, similar to what is found for the methanol masers in G9.62+0.20E.

2 OBSERVATIONS AND DATA REDUCTION

2.1 KAT-7

The 7-dish Karoo Array Telescope (Foley et al. 2016) was built as an engineering prototype for the 64-dish MeerKAT array in the Karoo region of the Northern Cape, South Africa. It consists of seven 12 m diameter dishes with prime focus linearly polarized receivers covering a frequency range of 1.2–1.95 GHz. It is a compact array, with a maximum baseline of 186 m and shortest baseline of 26 m. The system temperature of the antennas is approximately 30 K, and aperture efficiency is on average 65 per cent.

The OH maser monitoring observations started during the early stages of spectral line commissioning on KAT-7 in 2013 February. We used the c16n2M4k correlator mode, which gives a velocity resolution of 68 m s^{-1} at the OH rest frequencies. Since 2013 May, observations at 1665 and 1667 MHz were interleaved in a single schedule block using an LST-based scheduling mechanism, which ensures consistent uv coverage from one observation to the next and ensures that observations at both the frequencies are executed quasi-simultaneously. Prior to this, observations at each frequency were scheduled separately, preferably within the same day. The total integration time on source at each frequency was initially 20 min and subsequently increased to up to 50 min for the weekly monitoring programme and up to 80 min for the daily observations whenever possible. Daily observations during predicted flares were dynamically scheduled subject to telescope availability. Not all

antennas were always available, and integration time was increased when possible to compensate. The typical rms noise achieved ranges from 0.15 to 0.2 Jy. The typical beam size is ∼3 arcmin, thus the masers are unresolved and the relative positions of the masers cannot be measured due to the poor resolution.

PKS 1934–638 – the flux and bandpass calibrator – was observed for 5 min every hour. PKS 1730–130 was used as the gain calibrator and was observed once every 10 min for 1 min.

The data were calibrated following standard interferometric calibration procedures using CASA (McMullin et al. 2007). The bandpass response turned out to be stable in time, so all scans were combined to produce a single bandpass calibration table. In order to avoid introducing noise from the bandpass calibration into the spectrum (the continuum emission is similar in strength to the bandpass calibrator) the bandpass solution was smoothed using a third-order polynomial in both phase and amplitude. We were unable to obtain a reliable polarization calibration in the narrow-band mode due to insufficient signal to noise on the polarization calibrator 3C 286, so only the Stokes I product is considered here.

KAT-7 has a 1 square deg field of view and excellent sensitivity to low surface brightness emission. This results in a complex continuum image. Spectral line data cubes were imaged after continuum subtraction in the *u–v* plane. The sheer volume of the data necessitated automated data reduction and imaging. The first 'quick-look' image cubes produced had imaging artefacts (spurious source detections in isolated channels) and higher rms noise than expected in some channels. To address this problem, a deep image was made of the field by combining all available observations at the time – some 60 h of data on-source – in order to optimize the imaging parameters. There are five spectral line sources in the field of view, including a deep absorption feature, which were fully characterized to determine the appropriate velocity ranges for continuum subtraction, and to create a velocity-dependent CLEAN mask for non-interactive image deconvolution. The clean threshold was determined by measuring the rms noise in an emission-free channel. This approach led to much better and more consistent imaging quality even when uv coverage was reduced.

Data quality was severely compromised by solar interference during December and early January when first the gain calibrator and then the target were less than 12 deg from the Sun. We have discarded all data taken during this period.

2.2 Single-dish observations

Concurrent monitoring of the methanol and water masers was done using the Hartebeesthoek Radio Astronomy Observatory (HartRAO) 26 m telescope, subject to scheduling constraints.

Flux calibration at 6.7 and 12.2 GHz was done by daily drift scans on Virgo A and Hydra A using the flux scale of Ott et al. (1994). Amplitude corrections due to pointing errors were calculated by offset observations to the east–west and north–south half-power points. Bandpass calibration at 6.7 and 12.2 GHz was done by frequency switching, while position switching was done at 22 GHz to accommodate a potentially wider velocity spread. The pointing offsets at 22 GHz were greater than half a beamwidth at times, making it impossible to derive reliable amplitude correction since we detect the source in only one or two of the offset pointing positions. These observations have been discarded from the time-series. The 22 GHz flux densities were also corrected for atmospheric absorption using water vapour radiometer and environmental data. Jupiter was used as a flux calibrator.

3 RESULTS

Fig. 1 shows the spectra and range of variation of the OH masers at 1665 and 1667 MHz, the methanol masers at 6.7 and 12.2 GHz, and the water masers at 22 GHz. Variability is seen in the same velocity ranges for the methanol and hydroxyl transitions, between 1 and 3 km s^{-1}. The water masers are highly variable but have a different and larger velocity range.

3.1 Hydroxyl maser time-series

Fig. 2 shows the continuum image of the field with locations and identification of spectral line sources marked in red. Note that primary beam correction has not been applied to this image. At L band, we are detecting optically thin, evolved H II regions. Continuum emission is visible at the G9.62+0.20 site and is most likely dominated by components A and B (Garay et al. 1993), which are more evolved and extended H II regions in the complex.

Time-series were generated by fitting a two-dimensional Gaussian to channels of interest in the image plane. The uncertainty in the measured amplitude was calculated by measuring the rms noise in an outer quadrant of the image for that channel. We generated time-series for all velocity channels that had amplitudes greater than 3 times the rms noise. Figs 3 and 4 show the time-series for the 1665 and 1667 MHz data, respectively. The KAT-7 data suffer from heavy spectral blending, which could not be resolved by fitting individual Gaussian components to the spectra. Instead, we plot the measured flux density in each channel. We have grouped channels by visual inspection of both the spectral structure and the characteristics of the variability, which appears markedly different as we move between spots in the general star-forming region. The most notable behaviour is seen in the 1667 MHz transition in the peak velocity channels at ∼1.7 km s^{-1}. These features show a drop in intensity at the time that the methanol masers start to flare, followed by a sharp rise, and a gradual decay. In contrast, the features at ∼2 km s^{-1} show a flare profile that is more similar to that of the methanol masers.

3.2 Comparison with VLBI spectra and radio continuum positions

Since the individual hydroxyl maser spots cannot be resolved by KAT-7 and there are multiple spots with overlapping velocities, we inspected the VLBI spectra more closely to see if they could be correlated with the temporal and velocity behaviour seen in the KAT-7 data. The radio continuum source E appears to have two components – E1 is the stronger peak over which the methanol masers are centred, while E2 is one-fifth of the strength of E1 and is located ∼1000 au in projection to the north-east (see Sanna et al. 2015).

Fig. 5 shows the maser spotmap from Sanna et al. (2015), with the zoomed insets on the various OH maser clumps. The OH masers are not co-located with the methanol masers; instead they are distributed in several clumps around the region. The clump to the north-east is on the far side of component E2. Other clumps are distributed offset from the peak of E2 to the south-east, south, and west. The water masers are located between E2 and E1. It is also known that not all of the methanol masers flare (Goedhart et al. 2005), so comparison of the maser positions and their time-dependent behaviour may help to narrow down the origin of the periodic behaviour.

Figs 6 and 7 show the VLBA spectra, with the KAT-7 spectra taken at the closest epoch (2013 July 16) for a comparison. These
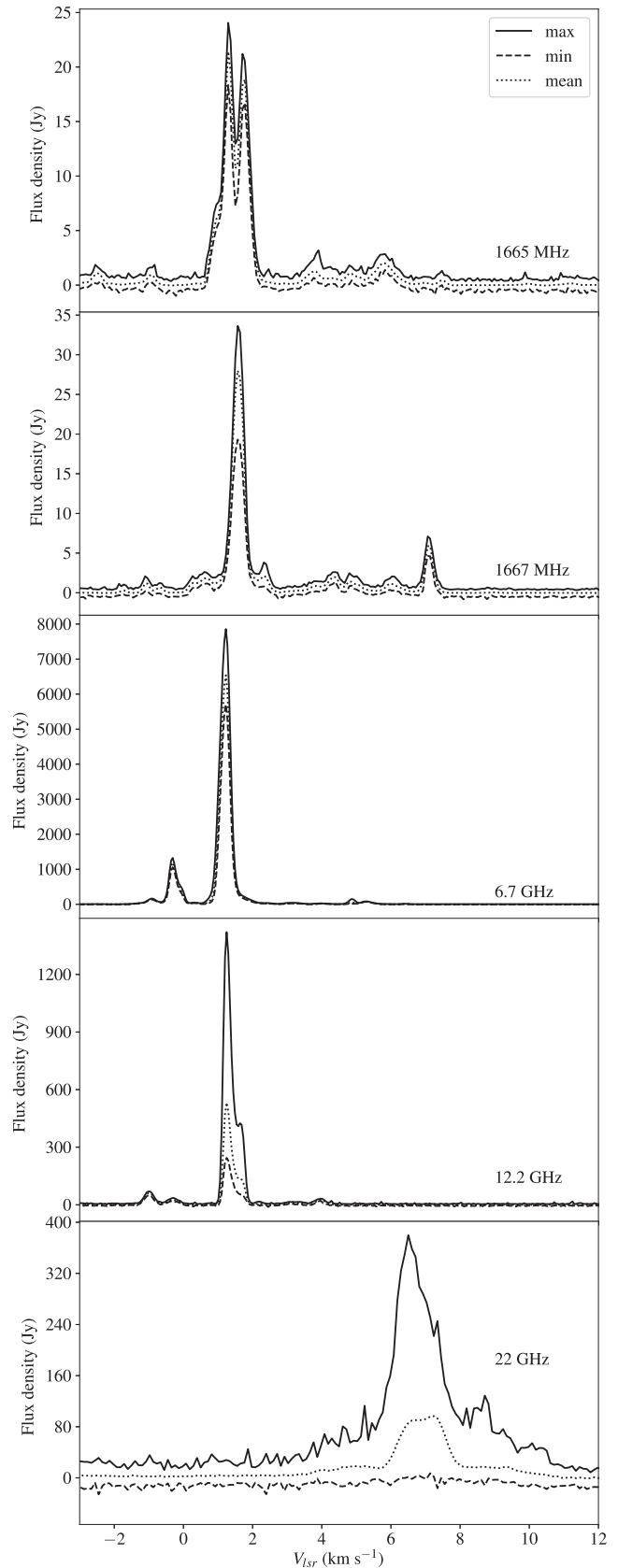

Figure 1. Spectra of the maser transitions monitored, showing the range of variation in each velocity channel.
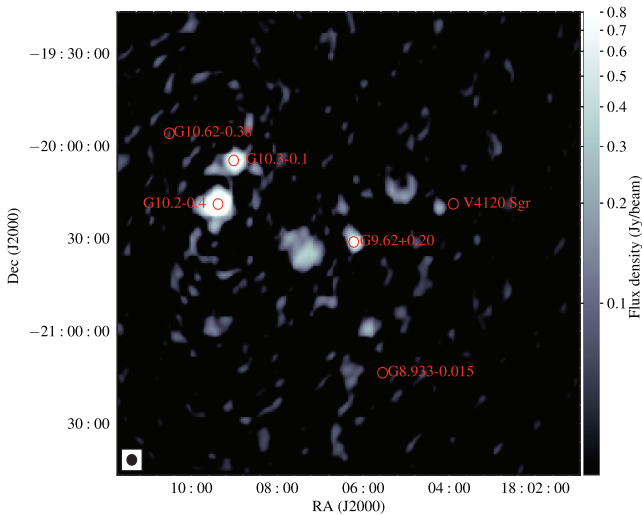
Figure 2. Overview of sources detected in the field. The colour scale shows the continuum image. The locations of spectral line sources are indicated by the red circles. The size of the circles indicates the synthesized beam size.

spectra are used to inform the allocation of spectral channels to mapped features. The following discussion will work through the enumerated panels in Figs 3 and 4. Panel 'a' covers velocities in the range 0.67–1.08 km s^{-1} (the shoulder on the 1665 MHz spectrum) and shows relatively constant flux densities throughout the monitoring period. These channels may be part of features 18/19 in the western group but the VLBI spectra show a single channel of 2.5 Jy in this velocity range, while the KAT-7 spectra show far more flux. It is not completely clear where panel 'b' channels originate. It may be a blend of spatially separate features. The velocity range covered by panels 'b' and 'c' – 1.15–1.36 km s^{-1} – is the same as that of features 17, 18, and 19 in the western group; however, the VLBI spectra recover significantly lower flux. It may be that the weak indication of flaring behaviour in panel 'c' is spectral blending with features 12 and 13 shown in panel 'd', and that the western group does not flare. The features in panel 'e' are unambiguously in the eastern group. Panel 'e' probably shows the blending of features 12/13 with features 18 and 19 in the west. In panel 'f', note the slight rise in flux density at 1.9–2.04 km s^{-1} during 2014 May–June and a possible similar event 2015 February, prior to the expected periodic flare. These features are in the same velocity range as 16, 18, and 19 to the west, or 20 and 21 in the east. The features in panel 'g', 3.62–3.9 km s^{-1}, appear to arise from a region ≈3 arcsec to the south of the peak of the H II region (Fish et al. 2005) and are not shown in Sanna et al. (2015). These features do not show any sort of correlated variability with the other masers.

Now to consider the 1667 MHz transition. Here the spectrum is simpler and the variability much more pronounced. Panel 'h' does not show any significant variation. It is not entirely clear where this emission arises since the VLBI spectra at this velocity range, 1.16–1.38 km s^{-1}, do not recover much flux. It could belong to features 4, 5, or 10, all of which are in the south-eastern group. Panel 'i' in the range 1.44–1.78 km s^{-1} shows very well demarcated drops in intensity, which occur at the onset of the methanol flare, as we will show in the next section. After the 'dip', the masers increase in strength to a level higher than the pre-flare level, then slowly recover over a period of several months. Features in this velocity

range include 1, 2, 4, 5, 7, 9, and 10. However, considering peak flux densities the contribution must be predominantly from features 1, 2, 7, and 9 that are in the east. Panel 'j' does not show much variation. This velocity range, 1.85–2.05 km s^{-1}, may be covered by features 7 and 9 but it is not clear why they would not flare if all the other masers in this region are flaring. Panel 'k' shows very pronounced flaring behaviour in the velocity range 2.12–2.4 km s^{-1} but it is unclear where these features are in the VLBI map – they could be part of 7 and 9 or 4 and 5 in the south-east. The features in panel 'l', as with panel 'g', arise from a region 3 arcsec to the south (Fish et al. 2005).

To summarize, the most variable features appear to be in the eastern group, closer to H II region component E2 and it is likely that none of the other OH maser groups are flaring.

3.3 Comparison of OH and methanol maser flare profiles

As already noted above, the OH maser flares have a 'characteristic' dip in the flux density before the flare. Such behaviour has not been reported for the methanol maser flares. In Fig. 8, a more detailed comparison between the OH and methanol maser flares is shown. The dip is seen to be significantly more pronounced for the 1667 MHz maser than for the 1665 MHz maser. It is rather interesting to note that for the 1667 MHz maser the onset of the dip is very near to the start of the 12.2 GHz maser flare. After the dip, the OH masers increase to a maximum after which they decay to the same level as before the onset of the 12.2 GHz maser flare. The time intervals between the peak of the 12.2 GHz maser and when the 1665 and 1667 MHz masers reach their maxima are about 23 and 13 d, respectively.

Given that after reaching a maximum, the OH masers recover to the same pre-flare level, a behaviour also seen for the methanol masers, we also tried to fit the decay part of the OH masers with equation (A7) of van der Walt et al. (2009) as well as to the decay of the 12.2 GHz methanol maser flare shown in Fig. 8. The fits are shown as the blue solid lines in Fig. 8. It is seen that for all three masers the decay of the masers is described very well by equation (A7) of van der Walt et al. (2009). Assuming that the decay of the masers is indeed related to the recombination of a partially ionized hydrogen plasma, the fit allows us to obtain estimates of the quiescent state electron density ($n_{e, \star}$) as well as the ratio (u_0) of the electron density from where the recombination started and $n_{e, \star}$. The values of these two quantities obtained from the fits are shown in the respective panels of Fig. 8. The derived quiescent state densities range from 5.7×10^5 cm^{-3} for the 12.2 GHz maser at 1.25 km s^{-1} to 1.54×10^5 cm^{-3} for the 1665 MHz OH maser. The order of magnitude of these densities is what is expected for very young H II regions. It is also seen that for the OH masers the value of u_0 as found from the fit is only 1.07, in agreement with the small amplitude of the flares. For a comparison, $u_0 = 1.85$ for the strong 12.2 GHz flare.

3.4 Water maser monitoring

Fig. 9 shows a dynamic spectrum of the water maser observations. While the masers are variable, there does not appear to be any particular correlation with the methanol or hydroxyl, but the time coverage during the 2013 September flare is extremely sparse due to bad telescope pointing. There are some transient features at ∼5 and ∼8 km s^{-1} in the second flare cycle, which also appear to have slight changes in peak velocities very typical of water masers in an outflow.
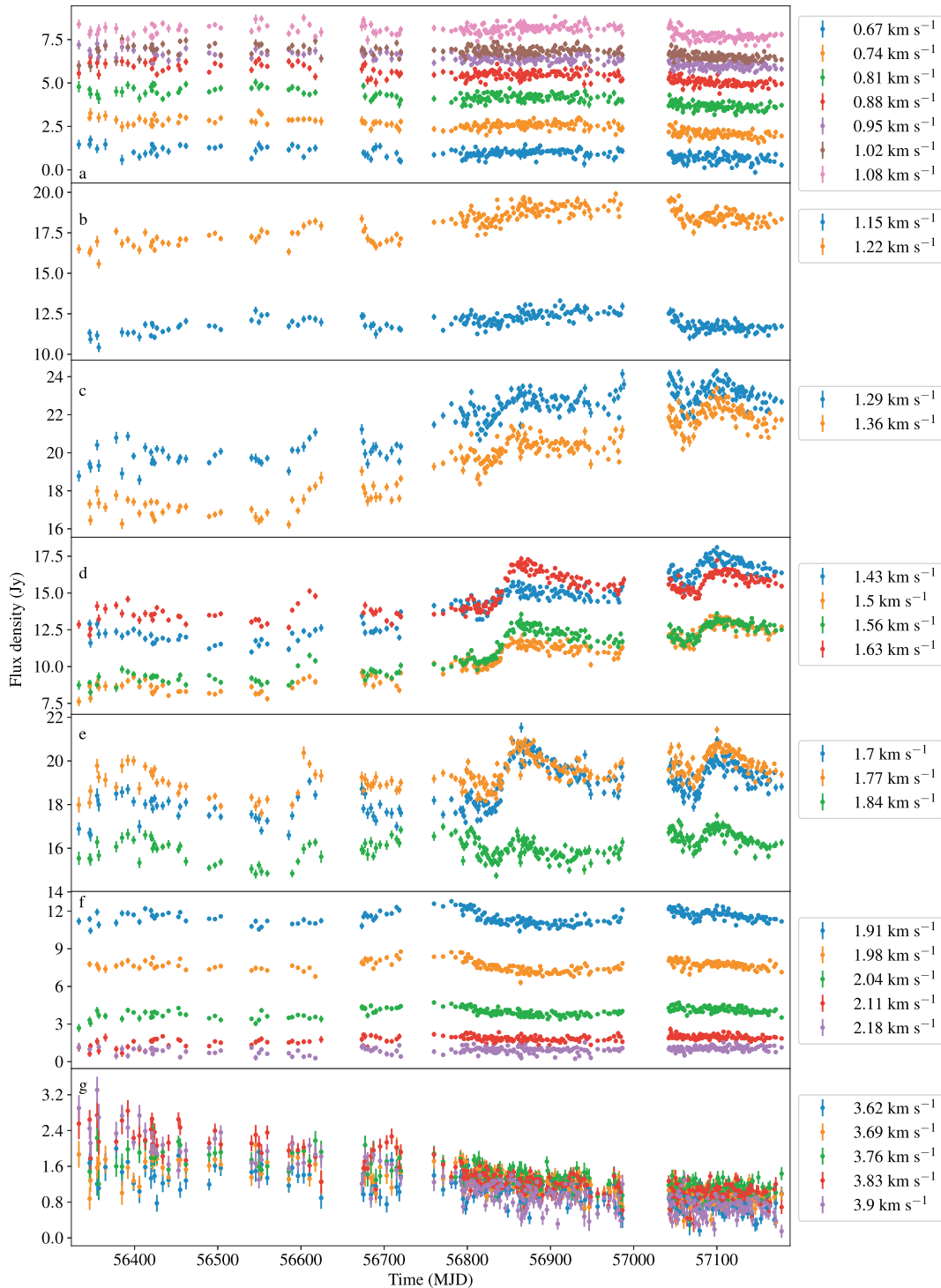
Figure 3. Time-series of individual velocity channels for the 1665 MHz OH masers. The plots have been split across channels to aid in visual identification of correlated behaviour.

In Fig. 10, we show a more detailed comparison between the time-series of the water and 12.2 GHz methanol masers between MJD 56700 and 57400. It is seen that the duration of the water maser flare covers a time interval approximately equal to the period of the 12.2 GHz flares. The water and methanol maser flares do not seem to be related in the same way as seems to be the case for the OH and methanol maser flares.

4 DISCUSSION

There are quite a number of interesting aspects to note in G9.62+0.20. We first note, using fig. 1 of Sanna et al. (2015), that, in projection, the periodic methanol and OH masers are located approximately 330 and 1930 au from the continuum peak of the VLA A-array 7 mm emission. Although there are OH masers located

Figure 4. Time-series of individual velocity channels for the 1667 MHz OH masers. The plots have been split across channels to aid in visual identification of correlated behaviour.
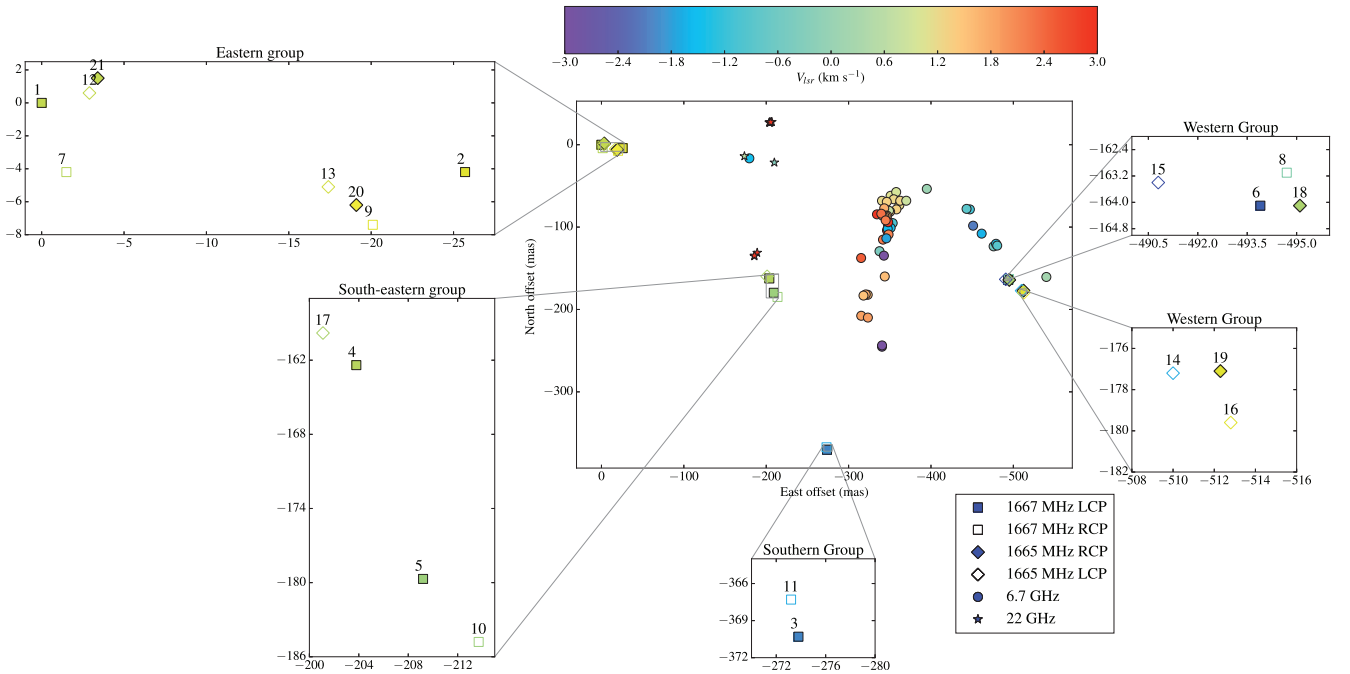
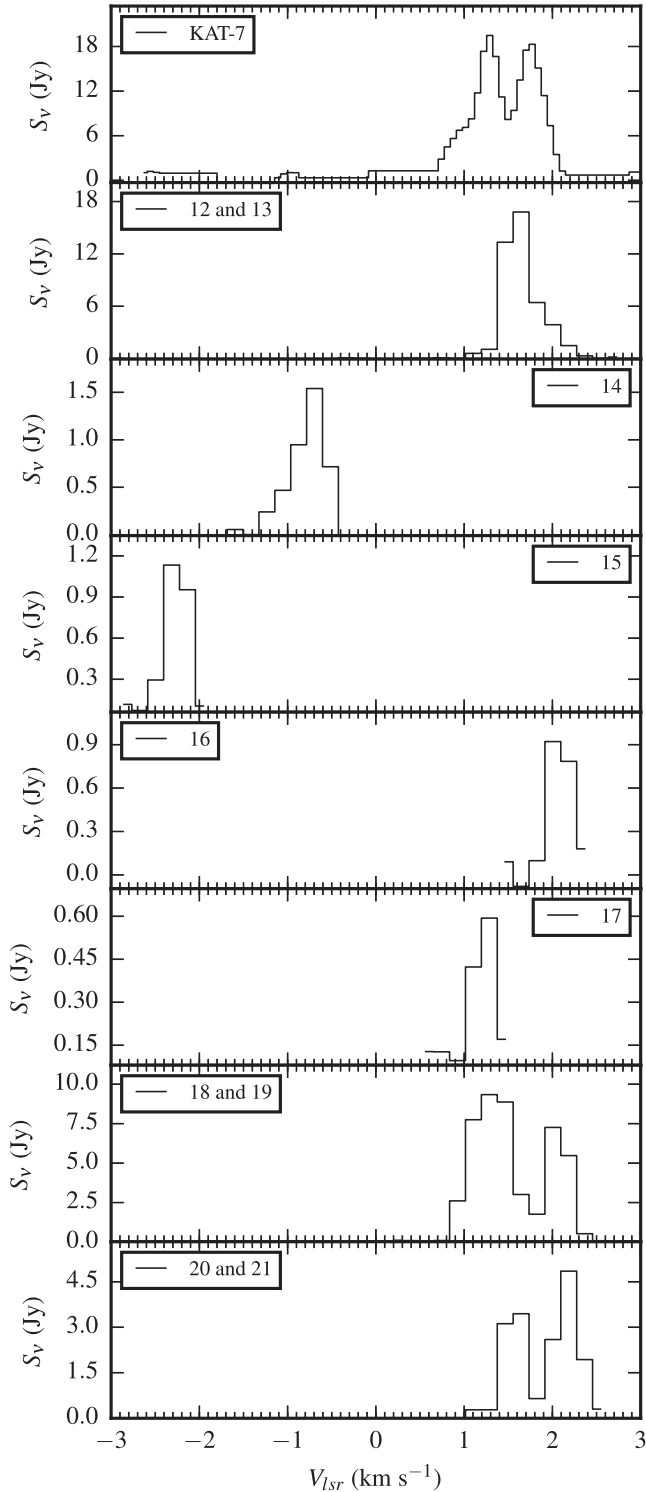**Figure 5.** Maser spot positions as reported in table 2 of Sanna et al. (2015).

Figure 6. Spectra of individual 1665 MHz maser features from Sanna et al. (2015). The top panel shows the KAT-7 spectrum from the nearest epoch (2013-07-16) 14 d later.

closer to the continuum peak, these do not appear to be periodic at all. The question then is why the periodic OH masers are located so much further than the periodic methanol masers from the peak of continuum. As shown above, equation A7 of van der Walt et al. (2009) provides a very good fit to the decay of the 12.2 GHz methanol maser flare. The implication is that the variation in the
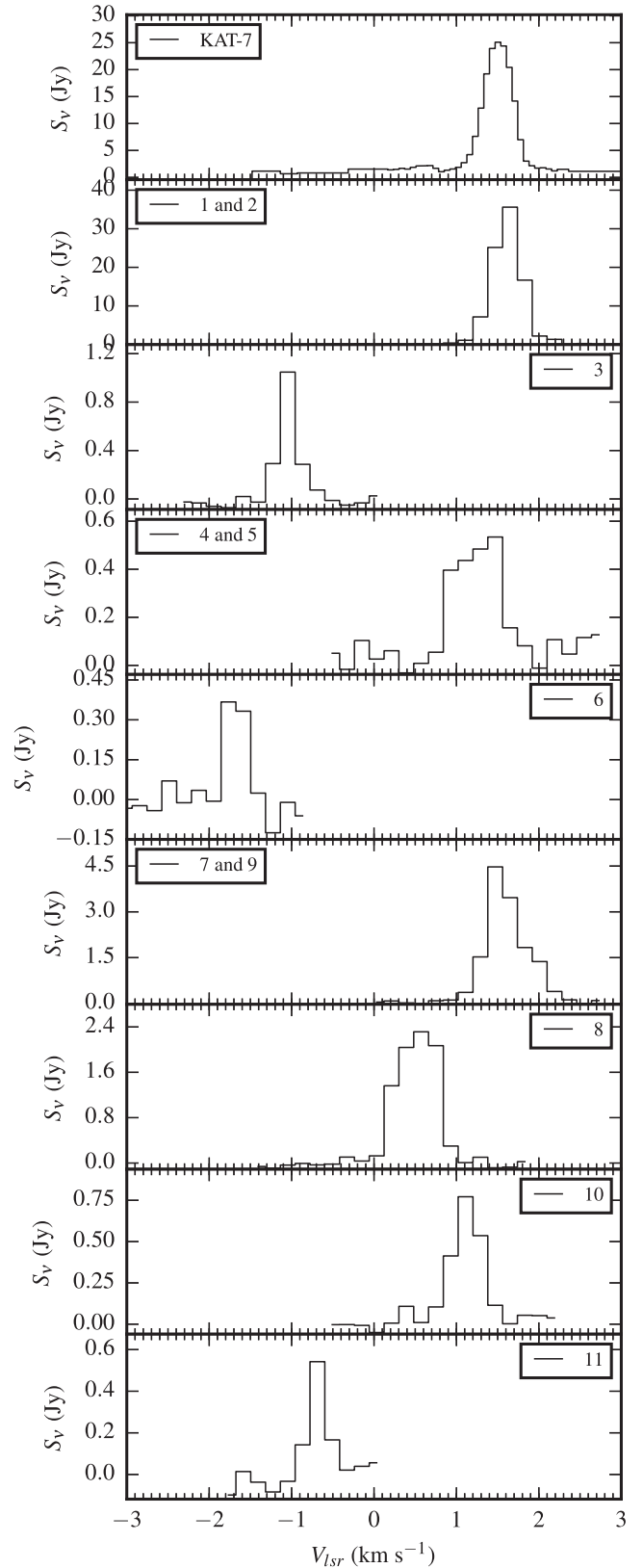

Figure 7. Spectra of individual 1667 MHz maser features from Sanna et al. (2015). The top panel shows the KAT-7 spectrum from the nearest epoch (2013-07-16) 14 d later.
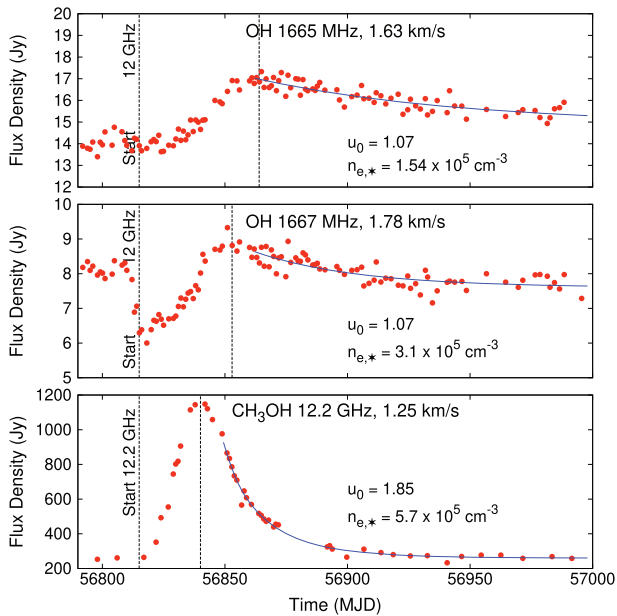
Figure 8. More detailed comparison of the profiles of the OH and methanol maser flares. The solid blue lines are the fits of equation A7 of van der Walt et al. (2009) to the decay of the flares. See van der Walt et al. (2009) for the interpretation of u_0 and $n_{e, \star}$.

electron density occurs at such a position that the H II region is optically thin for outward propagating 12.2 GHz photons in the direction of the masing gas. Since the optical depth is proportional to $\lambda^{2.1}$, it follows that at the projected position of the periodic methanol masers, the optical depth at 1665 MHz is about 65 times greater than at 12.2 GHz. If, for example, the optical depth at 12.2 GHz is 0.1, it means that it is 6.5 at 1665 MHz and therefore that all variability will be damped due to absorption in the H II region. Qualitatively, it is therefore expected that, if there are periodic OH masers, these will be located further from the core of the H II region compared to the periodic methanol masers. This might explain the relative projected positions of the periodic methanol and OH masers in G9.62+0.20E.

Perhaps the most intriguing aspect of the periodic OH masers in G9.62+0.20E is the pronounced sharp decrease (dip) in the maser flux density before the 'flare'. That the dip is a real feature is clear from the fact that it is seen in two flares and is also present in the 1665 MHz masers. As noted above, the periodic methanol masers do not show this behaviour. If, as proposed by van der Walt et al. (2009), van der Walt (2011), and van der Walt et al. (2016), the periodicity of the methanol masers in G9.62+0.20E is driven by a colliding-wind binary system and that the flares are due to changes in the background free–free emission from the H II region, it is required that the dip should also be explained within the same framework. We consider two possibilities.

(a) *The periodicity is due to a colliding-wind binary system (CWB) associated with component E1*: Although no quantitative explanation can be given, qualitatively we note the following. First, from the maps of Sanna et al. (2015) it is seen that the periodic OH masers are projected significantly (~1600 au) further from the core of the H II region E1 than the periodic methanol masers. Should both masers amplify the free–free emission from the background H II region, it follows that they probe two completely different parts of the H II region. The ionization structure of a UCH II region as

calculated with the photoionization code CLOUDY (see e.g. van der Walt 2011) shows that partially ionized gas extends beyond the ionization front. Within the framework of the CWB scenario, the lower energy ionizing photons from the hot shocked gas are absorbed at the ionization front and give rise to the flaring of the methanol masers. Higher energy (>100 eV) photons, on the other hand, can propagate beyond the ionization front due to the significantly lower photoionization cross-section for H I. Ionization of hydrogen by these photons will result in higher average electron temperatures. In the optically thin case, the free–free emission is proportional to the volume emissivity, which, in turn, is proportional to $T_e^{-0.5}$. Raising the electron temperature of the plasma thus lowers the volume emissivity.

A *possible* explanation then for the dip in the 1667 MHz maser flux density is that, because of the higher energies of the ionizing photons, the electron temperature is raised significantly during the ionization event in the gas against which the OH maser is projected, resulting in a decrease in the free–free emission. After the pulse of ionizing photons has passed, the electrons cool to the equilibrium temperature giving rise to an increase in the free–free emission and therefore also in the maser emission. Simultaneous to the increase in the electron temperature, the electron density also increases due to the pulse of ionizing photons. The exact profile of the flare (which includes the dip) depends on the magnitude of the change in electron temperature, the cooling rate of the electrons, and the ionization rate associated with the pulse of ionizing photons. The observed peak of the OH maser flares therefore does not necessarily indicate the time of the peak of the pulse of ionizing photons as in the case of the methanol maser flares. The difference in time between the peaks of the methanol and OH maser flares might therefore not be due to a geometric delay only (see below) but also to other physical effects. The required change in electron temperature to explain the magnitude of the dip can be estimated by considering the ratio of flux densities of the 1667 MHz maser before the dip and at the minimum of the dip (Fig. 8). It then follows that the electron temperature has to be raised by a factor of 1.8 to explain the observed decrease in the maser flux density. Thus, for example, if before the dip the electron temperature was 5000 K, it has to be raised to 9000 K in order to explain the decrease seen in the maser flux density.

(b) *The periodicity is associated with component E2*: Given that the decay of all three masers is described very well in terms of the recombination of a hydrogen plasma, it is reasonable to assume that component E2 must then also be a periodic source of ionizing photons that influence the flux of seed photons for both the methanol and OH masers. Since the methanol masers are projected against E1, it is therefore required that the ionizing photons propagate from E2 to the position against which the periodic methanol masers are projected. However, it is clear from Sanna et al. (2015) that there is very little ionized gas associated with E2, which means that a significant fraction of the flux of the periodically produced ionizing photons will be absorbed close to E2. It is therefore difficult to see how a source of periodically varying ionizing photons located at E2 will influence that part of E1 against which the periodic methanol masers are projected.

Having excluded E2 as the driving source for the periodic methanol and OH masers, we finally note the following. From Fig. 8, it is seen that although the peak of the 1667 MHz flare lags that of the 12.2 GHz flare by about 13 d, the dip of the 1667 MHz maser occurs almost simultaneously with the onset of the 12.2 GHz methanol maser flare. In view of the above possible explanation for the dip, it seems reasonable to regard the onset of the 12.2 GHz flare
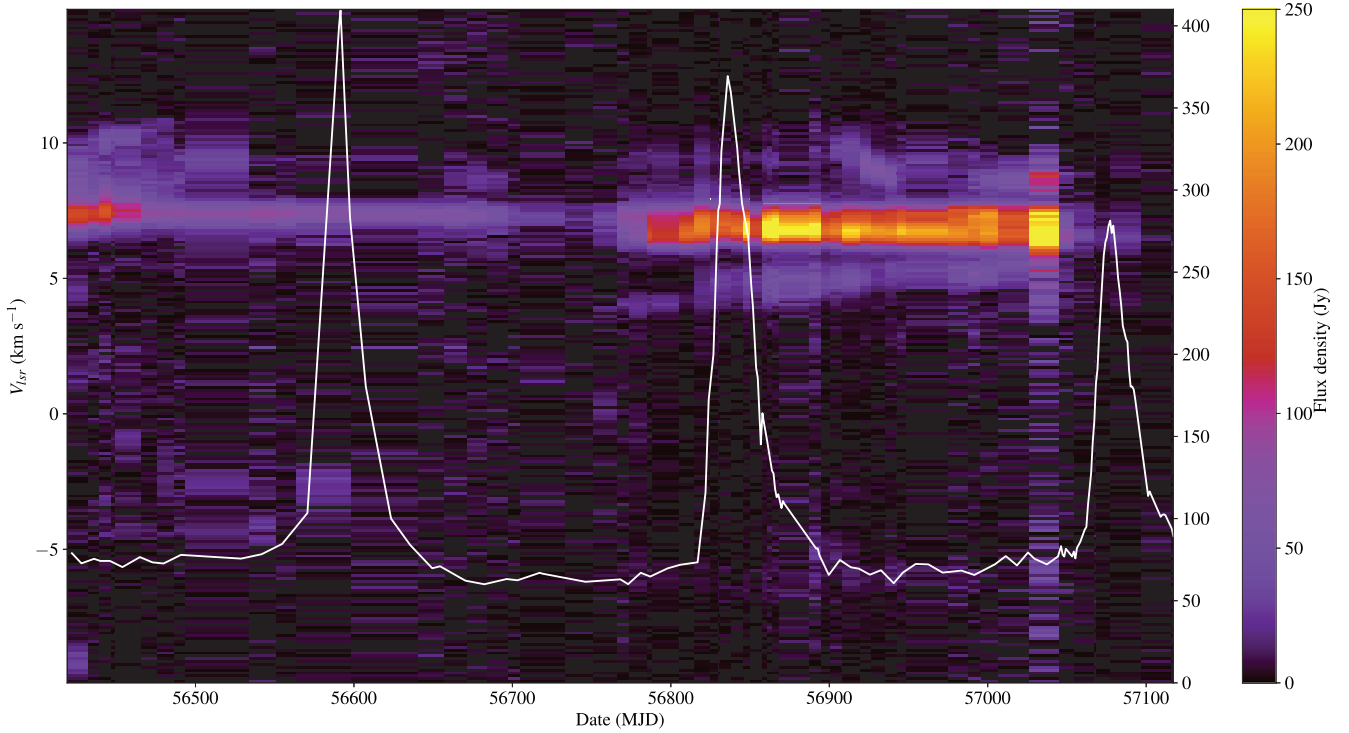
Figure 9. Flux density of water masers as a function of time and velocity in the colour-scale plot. The white curve is the 12.2 GHz methanol for a comparison.
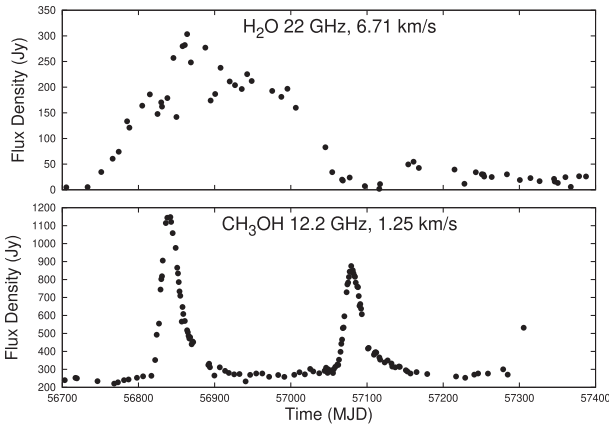

Figure 10. Comparison of water and 12.2 GHz methanol maser flares.

Figure 11. Simplified geometry for the locations of the periodic methanol and hydroxyl masers. The ionizing star is indicated by the star symbol. The 'surface' of the H II region is assumed to be flat. The methanol and hydroxyl masers, respectively, respond to changes in the free–free emission from points A and B.

and the almost simultaneous sharp decrease of the 1667 MHz maser flux density to be caused by the same ionization event. However, due to the difference in projected distances from the core of the H II region, we then expect the dip of the OH maser flares to be delayed by about 9 d with respect to the onset of the 12.2 GHz flare. Considering the very simple geometry in Fig. 11, the time difference between the methanol and hydroxyl flares is given by $\Delta t = (r_B - r_A + z_{OH} - z_{CH_3OH})/c$. For the present case $\Delta t \sim 0$, from which follows that $z_{CH_3OH} - z_{OH} \approx r_B - r_A$. Our observations of the methanol and OH maser flares therefore suggest that the masing region of the periodic 12.2 GHz methanol masers is located about 1600 au further from the 'surface' of the H II region into the molecular envelope compared to the location of the periodic OH masers.

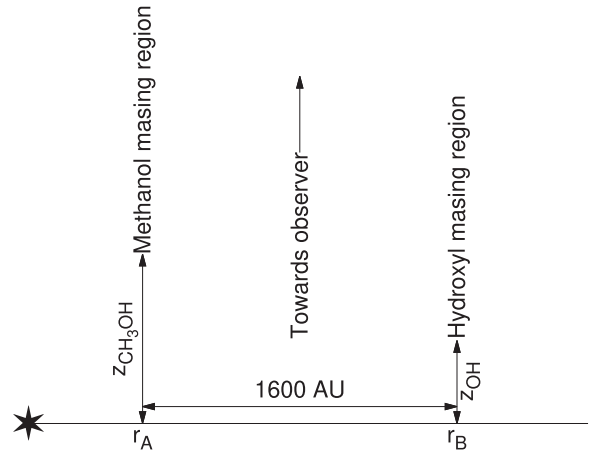As noted above, a water maser flare occurred that overlapped in time with a 12.2 GHz methanol maser flare. It seems as if a comparison between the water and methanol maser flares similar to that between OH and methanol masers cannot be made. Although the water maser flare overlaps in time with the 12.2 GHz methanol maser, the water maser flare clearly starts before the methanol maser flare. Also, the decay time of the water maser flare is significantly different from that of the OH and methanol maser flares and does not suggest any causal relation with the methanol and OH flares.

To our knowledge, the results presented above are the first conclusive observational evidence of periodic variability of OH masers associated with a high-mass star-forming region. Green et al. (2012) found an indication of periodicity in the OH masers

towards G12.889+0.489 (which has a 29.5 d period in methanol), but the time-series were too undersampled to obtain detailed cycle profiles and no contemporaneous methanol monitoring was done. It is interesting that the hydroxyl masers appear to undergo a drop in emission coincident with the expected minima of 6.7 GHz methanol masers but a key difference is that the hydroxyl masers do not show any flares. G12.889+0.489 also differs from G9.62+0.20E in that it has somewhat irregular flaring behaviour in the methanol, but shows a well-defined minimum, which seems to be periodic (Goedhart et al. 2009), while the peaks of the methanol flares can occur any time in an 11 d window. It is quite likely, given the short period and the difference in the methanol maser light curves, that a different mechanism is modulating the maser intensity. It would undoubtedly be of great benefit to our understanding of these phenomena to conduct intensive monitoring of both maser species through one 29.5 d cycle in this source.

5 SUMMARY AND CONCLUSIONS

We presented the first conclusive observational evidence for the periodic variability of OH mainline masers associated with a high-mass star-forming region. The 1667 MHz masers show a pronounced dip in flux density, which closely coincide with the onset of the 12.2 GHz methanol maser flare. The decay of the OH maser flares, similar to that of the methanol maser flares, can be described very well by the decrease in the free–free emission from the background H II region as expected from a recombining hydrogen plasma. A possible explanation, within the framework of the colliding-wind binary scenario, for the dip in flux density of the 1667 MHz masers is that it is due to an increase in electron temperature following the ionization of the outer regions of the H II region by photons with energy greater than about 100 eV. We also argued, within this framework, that the masing region for the periodic 12.2 GHz methanol masers is located about 1600 au further from the 'surface' of the H II region into the molecular envelope compared to the location of the periodic OH masers.

ACKNOWLEDGEMENTS

REFERENCES

Araya E. D., Hofner P., Goss W. M., Kurtz S., Richards A. M. S., Linz H., Olmi L., Sewiło M., 2010, ApJ, 717, L133
Cragg D. M., Sobolev A. M., Godrey P. D., 2002, MNRAS, 331, 521
Fish V. L., Reid M. J., Argon A. L., Zheng X.-W., 2005, ApJS, 160, 220
Foley A. R. et al., 2016, MNRAS, 460, 1664
Fujisawa K. et al., 2014, PASJ, 66, 78
Garay G., Rodríguez L. F., Moran J. M., Churchwell E., 1993, ApJ, 418, 368
Goedhart S., Gaylard M. J., van der Walt D. J., 2003, MNRAS, 36, L33
Goedhart S., Minier V., Gaylard M. J., van der Walt D. J., 2005, MNRAS, 356, 839
Goedhart S., Langa M. C., Gaylard M. J., Van Der Walt D. J., 2009, MNRAS, 398, 995
Goedhart S., Maswanganye J. P., Gaylard M. J., van der Walt D. J., 2014, MNRAS, 437, 1808
Green J. A., Caswell J. L., Voronkov M. A., McClure-Griffiths N. M., 2012, MNRAS, 425, 1504
Inayoshi K., Sugiyama K., Hosokawa T., Motogi K., Tanaka K. E. I., 2013, ApJ, 769, L20
Maswanganye J. P., Gaylard M. J., Goedhart S., van der Walt D. J., Booth R. S., 2015, MNRAS, 446, 2730
Maswanganye J. P., van der Walt D. J., Goedhart S., Gaylard M. J., 2016, MNRAS, 456, 4335
McMullin J. P., Waters B., Schiebel D., Young W., Golap K., 2007, in Richard A. S., Frank H., David J. B., eds, ASP Conf. Ser. Vol. 376, Astronomical Data Analysis Software and Systems XVI. Astron. Soc. Pac., San Francisco, p. 127
Ott M., Witzel A., Quirrenbach A., Krichbaum T. P., Standke K. J., Schalinski C. J., Hummel C. A., 1994, A&A, 284, 331
Parfenov S. Y., Sobolev A. M., 2014, MNRAS, 444, 620
Sanna A. et al., 2015, ApJ, 804, L2
Sanna A., Reid M. J., Moscadelli L., Dame T. M., Menten K. M., Brunthaler A., Zheng X. W., Xu Y., 2009, ApJ, 706, 464
Singh N. K., Deshpande A. A., 2012, in Booth R. S., Vlemmings W. H. T., Humphreys E. M. L., eds, Proc. IAU Symp. 287, Cosmic Masers – from OH to H0. Kluwer, Dordrecht, p. 93
Sugiyama K. et al., 2017, PASJ, 69, 59
Szymczak M., Wolak P., Bartkiewicz A., van Langevelde H. J., 2011, A&A, 531, L3
Szymczak M., Wolak P., Bartkiewicz A., 2015, MNRAS, 448, 2284
Szymczak M., Olech M., Wolak P., Bartkiewicz A., Gawroński M., 2016, MNRAS, 459, L56
van der Walt D. J., 2011, AJ, 141, 152
van der Walt D. J., Goedhart S., Gaylard M. J., 2009, MNRAS, 398, 961
van der Walt D. J., Maswanganye J. P., Etoka S., Goedhart S., van den Heever S. P., 2016, A&A, 588, A47

This paper has been typeset from a TeX/LaTeX file prepared by the author.